Actin-based propulsion of functionalized hard versus fluid spherical objects

# New Journal of Physics

# Actin-based propulsion of functionalized hard versus fluid spherical objects

**Vincent Delatour, Shashank Shekhar, Anne-Cécile Reymann, Dominique Didry, Kim Hô Diêp Lê, Guillaume Romet-Lemonne, Emmanuèle Helfer and Marie-France Carlier**

Cytoskeleton Dynamics and Motility, Laboratoire d'Enzymologie et Biochimie Structurales, CNRS, Avenue de la Terrasse, 91190 Gif-sur-Yvette, France
E-mail: romet@lebs.cnrs-gif.fr and helfer@lebs.cnrs-gif.fr

**Abstract.** The directed polymerization of a branched actin network against a functionalized surface drives cell protrusions and organelle propulsion in living cells. Solid microspheres or giant unilamellar vesicles, functionalized with neural Wiskott–Aldrich syndrome protein (N-WASP), initiate the formation of a branched actin array using actin-related protein 2/3 (Arp2/3) complex, when placed in a motility assay reconstituted with pure proteins. These systems are useful biomimetic models of actin-based propulsion that allow to address how the interplay between the physical properties of the functionalized surface and the dynamics of the actin cytoskeleton determines motile behavior. Both solid beads and deformable vesicles display either continuous or saltatory propulsive motions, which are analyzed comparatively; we show that the deformability of liposomes and the mobility of N-WASP at the lipid surface affect the dynamic and structural parameters of the actin meshwork. Our results indicate that beads and vesicles use different mechanisms to translate insertional polymerization of actin at their surface into directed movement: stress relaxation within the actin gel prevents the accumulation of filaments at the front of moving beads, while segregation of nucleators reduces actin polymerization at the front of moving vesicles.

**IOP** Institute of Physics  Φ DEUTSCHE PHYSIKALISCHE GESELLSCHAFT

**Contents**

## 1. Introduction

The polymerization of actin in branched filament arrays, organized by the neural Wiskott–Aldrich syndrome protein (N-WASP)–actin-related protein 2/3 (Arp2/3) machinery bound to the membrane, drives a large variety of motile processes of different morphologies, either protrusions (lamellipodia, invadopodia and filopodia), invaginations (phagocytic, macropinocytic and endocytic processes) or propulsive intracellular 'rocketing' of endosomes or bacterial pathogens like *Listeria*, or *Shigella* [1]–[4].

These processes result from the interplay of the actin meshwork with the surface-bound protein N-WASP. In these different cases forces are produced against a rigid object like a bacterium or a soft object like a membrane, in either a concave or convex geometry. The chemo-mechanical coupling between actin filaments and the N-WASP/Arp2/3 machinery therefore differs in all these processes, although the molecular reactions at the origin of force are identical, which gives an indication of the amazing adaptability of the actin nanomachine and its capacity to produce force in different environments.

The reconstitution of actin-based propulsion of *Listeria* in a minimum medium consisting of actin and four regulatory proteins [5] has enabled the physical mechanism of force production by growing actin filaments in these various cellular situations to be addressed. This assay demonstrated that the movement is powered by filament treadmilling and results from the balance between sustained site-directed creation of new barbed ends by branching mediated by surface-bound N-WASP, and arrest of filament growth by barbed end capping, thus regulating the number of filaments transiently growing and pushing against the surface. Filaments are attached to the surface during the branching reaction, then detached to allow the growth of the

two new filaments: the growing detached filaments push while the attached filaments pull on the surface (see [6]–[8] for reviews).

In the past years, the biomimetic motility assay was extended to compare the propulsive movement of either solid microspheres [9]–[11], similar to bacteria, on which nucleators (e.g. N-WASP) occupy fixed positions, and soft microspheres like oil drops [12, 13] or—closer to biological membranes—giant unilamellar vesicles (GUVs) [14]–[16]. In addition to their property of deformability, the two latter objects are fluid, i.e. nucleators can diffuse on the surface. The movement of these objects was observed either in cell extracts or in a reconstituted medium of purified proteins. Soft droplets or vesicles were deformed by the growing actin meshwork, exactly like actin-propelled endosomes in cells [17]. Based on these observations, it was shown that the actin gel pulls on the rear of the propelled object [12, 15, 16], suggesting that the ratio of pulling to pushing filaments should be greater in that region. This point has not yet been observed experimentally, illustrating that connections still need to be established between microscopic and mesoscopic scales in our understanding of actin-based motility.

The dynamic interactions of the functionalized surface and the growing branched actin array cannot be identical in the cases of rigid and fluid objects. The observed peculiar hopping behavior of solid beads and fluid objects has been explained, within the concept of filaments' transient attachment to the surface, by different mechanisms. The non-monotonous friction–velocity relation at the actin gel–bead interface was proposed to result in a stick–slip process [9], while the alternating homogeneous and segregated distribution of nucleators at the surface of oil droplets and vesicles was proposed to account for their hopping propulsion [13, 14]. Here, we analyze the hopping behavior of solid beads and GUVs and compare the mechanisms that lead to the establishment and the maintenance of directed movement in these two systems. We show that the generation of a non-isotropic actin structure around the object, which is necessary for directional movement, arises from the relaxation of elastic stresses in the gel built around the solid beads, whereas it stems from the anisotropic distribution of nucleators on the fluid surface of GUVs.

## 2. The activity of the surface-bound actin nucleator is affected by its interaction with the surface

In the cell context, the isolated N-WASP protein is folded in an almost inactive conformation, and activated by a large number of ligands in response to signaling. Activation physically exposes the catalytically active domain of N-WASP, called VCA, to its substrates i.e. Arp2/3 complex, a G-actin molecule and a filament. The ternary complex VCA-actin-Arp2/3 interacts with a 'mother' filament leading to the formation of a branch and the initiation of a lateral 'daughter' filament. In the branching process, the filaments are transiently attached to the surface via N-WASP, then released in solution where the two barbed ends grow [11, 18, 19].

When N-WASP was adsorbed at the surface of rigid microspheres, or bound to Ni-derivatized lipids via a N-terminal His-tag, it lost its sensitivity to standard activators like PIP2 [11] or Cdc42-GTPγS and branched filaments with the characteristics of the fully activated state. Hence, surface adsorption affects the structure and activity of the nucleator.

The VCA fragment, which is constitutively active in solution, remains active when bound to Ni-derivatized lipids via a N-terminal His-tag, but is inactive when adsorbed on carboxylated polystyrene microspheres. Other groups have however observed propulsion of non-carboxylated

polystyrene beads functionalized with GST-tagged VCA [20], suggesting that the GST-tag binds to the surface, and prevents noxious VCA–surface interactions.

## 3. The coordinated mechanical properties of the functionalized surface and of the branched actin meshwork determine the initiation and the maintenance of movement

### 3.1. Saltatory movement generates different kinetics and comet morphologies for GUVs and beads

A N-WASP-functionalized solid microsphere or liposome, once placed in the motility assay first initiates the growth of a dense spherically symmetric actin meshwork, by insertional filament branching and growth. A break of symmetry eventually takes place, a gap is formed in the actin gel, allowing the particle to escape from the actin shell. The particle is then propelled in the direction defined by the gap, by the growth of an actin tail on the opposite face. The subsequent movement is either continuous or saltatory. In saltatory propulsion, steady movement is not maintained, i.e. the particle slows down, re-initiates the formation of a quasi-symmetric actin shell and repeats the initial symmetry-breaking step over and over. It must be noticed here that the second and subsequent actin shells around the vesicles or the beads are never perfectly symmetrical, but weaker at the front, hence the initial direction of the movement defined by the gap in the first shell is partially conserved. Comparing the physical parameters of saltatory propulsion of solid beads and soft liposomes provides insight into the role of deformability of the surface in the mechanism of symmetry breaking.

We have monitored the saltatory movement of GUVs and microbeads comparatively. These assays were performed using a biochemical composition of the medium that favors the occurrence of GUV saltatory motion: 100 nM gelsolin and 50 nM Arp2/3 [14]. The 4.6-$\mu$m-diameter vesicle and the 10-$\mu$m-diameter bead shown in figure 1 (figures 1(A) and (B), respectively; movies 1 and 2 available from stacks.iop.org/NJP/10/025001/mmedia) are typical of saltatory behavior of vesicles and beads within the 3–10 $\mu$m diameter range that we explored. As can be readily observed on timelapse images in figure 1, the structure of the actin comet is very different in the saltatory regimes of a bead and a GUV. The dense actin regions in the comet tail, which are remnants of the quasi-spherical actin shells that were broken open, display different shapes and spatial periods (step-size of saltatory movement). The position of beads, as well as the position of the front and the rear of GUVs, were tracked as a function of time during saltatory propulsion. For the vesicle, the front and rear velocities and the derived deformation (vesicle length $L$ divided by its average diameter $D$) were averaged over five subsequent steps and plotted over one period (a plot of the front velocity over the full five steps is available as supplementary material from stacks.iop.org/NJP/10/025001/mmedia); for the bead, the instantaneous velocity is plotted over two subsequent steps.

Vesicle and bead in saltatory motion display a qualitatively similar behavior: they alternate between two regimes of slow and rapid movement, corresponding to the growth of the actin shell around the object and to the escape from the shell, respectively. However, beads never move faster than 3–4 $\mu$m min$^{-1}$ as they are expelled from the actin shell, whereas vesicles can reach velocities higher than 10 $\mu$m min$^{-1}$, peaking sharply immediately following the maximum deformation of the vesicle. At the peak velocity, the rear of the GUV is released from the actin shell, allowing the rapid relaxation of GUV deformation. These data indicate that the energy stored in deformable vesicles is rapidly released and used to enhance velocity.
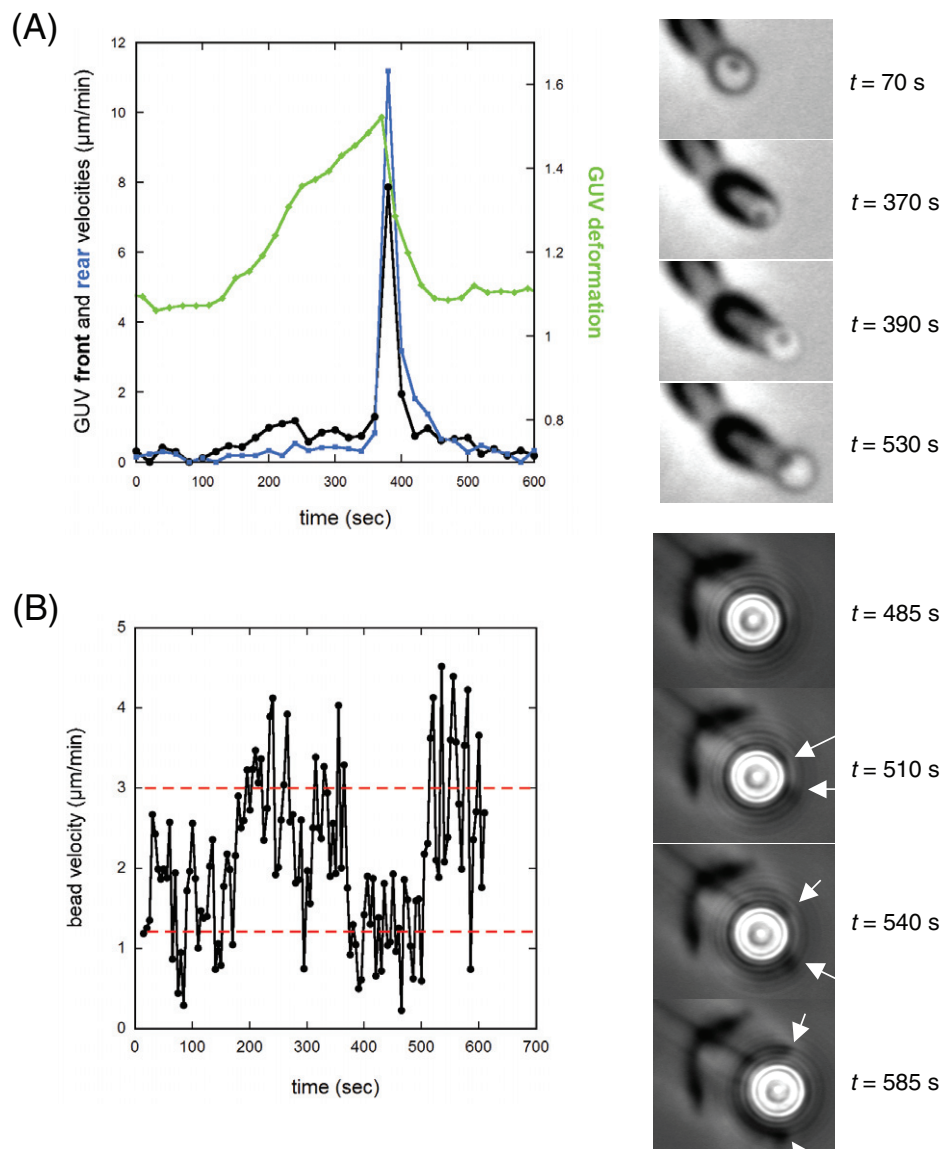
**Figure 1.** Kinetic analysis of a cycle during saltatory periodic motion. The saltatory movements of a 4.6-$\mu$m-diameter vesicle, taking steps of 8.3 $\mu$m every 540 s (A), and of a 10-$\mu$m-diameter bead, taking steps of 10.6 $\mu$m every 370 s (B) were tracked, using phase contrast microscopy. On the right are corresponding time-lapse images. Corresponding movies (1 and 2, respectively) are available from stacks.iop.org/NJP/10/025001/mmedia. (A) The velocities of the front (black line) and the rear (blue line) of the vesicle and the deformation (green line), defined as the vesicle length-to-average diameter ratio ($L/D$) are plotted over one period. Measurements were made at 20 s intervals, and averaged over five consecutive steps. (B) Tracking of two consecutive steps of the bead. The noise is due to pixel-limited accuracy. The red dashed lines indicate the average velocities of the slow and fast phases of the second step. Data points are 5 s apart. The arrows in the images point to the edges of the opening actin shell.

**IOP** Institute of Physics  **ⵁ**DEUTSCHE PHYSIKALISCHE GESELLSCHAFT

Objects in periodic saltatory movement repeat a sequence of events that are reminiscent of the initial expulsion. As we will see in the next section, the morphology differences in the saltatory movement of beads and GUVs reflect the differences in their respective symmetry-breaking processes.

### 3.2. Differences in the symmetry-breaking mechanism of GUVs and beads

As reported by other groups, the actin shell growing around a spherical object accumulates mechanical stress as it is compressed radially and stretched tangentially [10, 21]. The actin shell growing around a bead breaks open at the outer surface and straightens as stress accumulated in the actin gel is relaxed [10, 20], [22]–[24]. van der Gucht *et al* [10] published a detailed analysis of the symmetry breaking process that occurs at the outer surface of the actin gel. We found that functionalized GUVs break symmetry by a different mechanism. The pressure generated at the surface of the vesicle by the radial insertional growth of actin filaments pushes the vesicle against a region of the actin shell that certainly opposes a weaker mechanical resistance: in contrast with the case of the bead, the actin shell around the vesicle becomes thinner from the inside, as shown in the kymograph of figure 2(A) (see also movie 3, available from stacks.iop.org/NJP/10/025001/mmedia). This is followed by the creation of a hole that gets progressively wider, through which the vesicle escapes.

Polymerization occurs at the inner edge of the actin gel (the GUV surface), while depolymerization takes place mainly at the outer edge. The thinning of the actin shell at the front of the vesicle could result either from a local lesser extent of polymerization at the inner surface of the gel, or from mechanical disruption of the gel at the outer edge, where tensile stress is the strongest and could theoretically enhance depolymerization [25]. To discriminate between the two possibilities, we have performed two-fluorophore experiments, which allow to distinguish the inner from the outer region of the actin shell (see appendix). It was observed that for vesicles that have just broken symmetry, the outer region of the gel (green fluorescence, and solid green line in figure 2(B)) maintains a constant thickness while the inner region (red fluorescence and solid red line in figure 2(B)) gets thinner at the front, demonstrating that symmetry-breaking takes place at the vesicle–actin gel interface. Therefore it is the radial compression rather than the tangential stretching of the actin gel that initiates symmetry-breaking in the case of GUVs. Later after symmetry-breaking, as the front of the actin gel continues to thin, its outer region joins the inner region in the thinning process (figure 2(C)). This suggests that the tensile (tangential) stress, which should increase as the gel becomes thinner [25], could contribute by driving the thinning of the outer region after symmetry has been broken.

It should be noted that while a high surface density of N-WASP is required for the beads to break symmetry and initiate movement (less than 10 nm between nearest neighbors [11], 6 nm in the present study), a much lower density of N-WASP (23 nm between nearest neighbors) is sufficient for GUVs (see appendix). The mobility of N-WASP in the bilayer enhances its activity by facilitating its encounters with actin filaments, hereby favoring the branching reaction. The autocatalytic nature of the branching process may also lead to local inhomogeneities in N-WASP density. As a result, regions of lower N-WASP densities could develop, accompanied by regions of lower polymerization. Such regions would hence be mechanically weaker (i.e. have a lower Young's modulus) than the rest of the actin shell, and locally fail to balance the vesicle's osmotic pressure. This interplay between membrane and actin dynamics would lead to the local thinning of the actin shell (and GUV deformation) observed during symmetry-breaking.
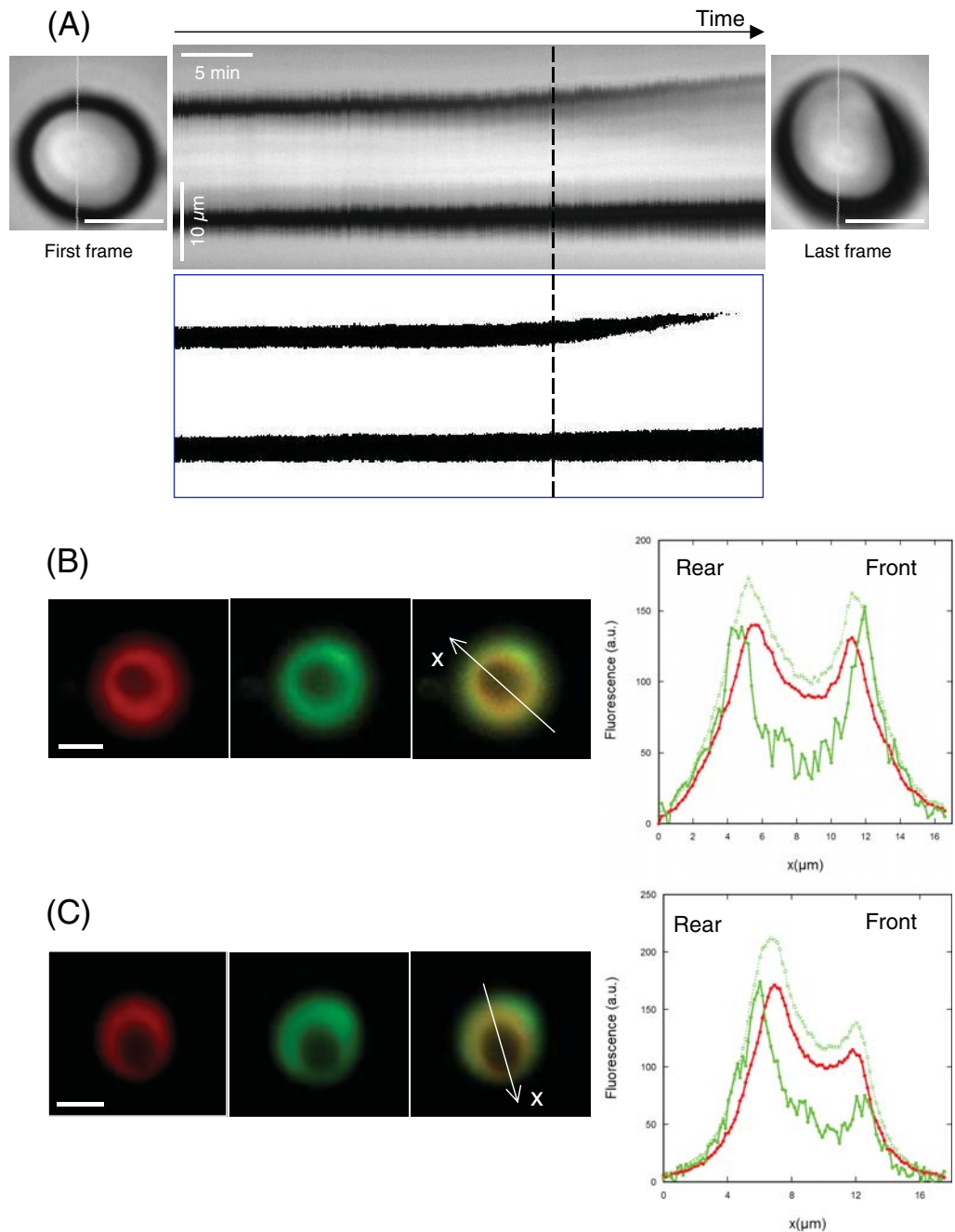
(A)

Time

5 min

10 μm

First frame

Last frame



(B)

Rear    Front

x

(C)

Rear    Front

x

**Figure 2.** See caption on next page.

When the surface density of N-WASP is very high, beads generate multiple comets derived from multiple fractures in the gel outer surface (figure 3(A) and [26], similar to phenotypes observed at low concentration of capping protein [23]). In contrast, at high N-WASP density, GUVs are not able to break symmetry, and eventually collapse under the pressure exerted by the actin shell (figure 3(B)). This collapse could be due to leakage of the GUV under pressure, as recently proposed for other liposomes growing actin gels from their surface [27] .

**Figure 2.** Vesicles break symmetry at their surface. (A) Kymograph showing the thinning of the actin gel at the front of the GUV. The actin shell around a 14.6-$\mu$m-diameter vesicle was observed in phase contrast (5 s between images, 500 images). Top panel: the derived kymograph was measured along the gray line drawn on the vesicle (movie 3 available from stacks.iop.org/NJP/10/025001/mmedia). Scale bar $= 10\,\mu$m. The dark zones in the kymograph correspond to the actin shell; the brighter central region corresponds to the vesicle. Bottom panel: a threshold was applied to the kymograph to better show the changes in the actin shell. The rear of the actin shell (bottom of kymograph) thickens constantly, while the front of the actin shell (top of kymograph) becomes thinner from the inside after symmetry-breaking (indicated by dashed vertical line), as the vesicle elongates and pushes against it. After symmetry-breaking, the inner and outer limits of the front actin shell move steadily forward at $0.328 \pm 0.012$ and $0.104 \pm 0.003\,\mu$m min$^{-1}$, respectively. (B) and (C) Evidence that thinning of the actin gel begins at the GUV–actin interface. A GUV is put in a motility medium containing Alexa-488(green)-labeled actin for 15 min, then diluted into a medium containing Alexa-568(red)-labeled actin (see appendix). The older, outer region of the actin shell contains only green actin, while the more recent, inner region contains both red and green actin. Left to right: red fluorescence, green fluorescence and merged images. Scale bar $= 5\,\mu$m. The images are scanned along the white lines ($x$-axis) to derive the curves on the right panel: the red signal (inner region, solid red line), the green signal (dotted green line), and the green signal coming only from actin polymerized before the addition of red actin (outer region, solid green line). (B) and (C) represent typical samples at different times after symmetry breaking. (B) shows a GUV just after symmetry breaking (12 min after mixing with red actin). The inner region of the actin shell is 32($\pm$5)% thinner at the front than the rear, while the outer region remains as thick ($\pm$4%) at the front than the rear (see appendix). (C) shows another GUV, a little bit later after symmetry has been broken (13 min after mixing). Both the outer and the inner regions of the actin shell are thinner at the front.

After symmetry-breaking, the actin shell around the bead opens up and straightens, as stress accumulated in the actin gel is relaxed. The expansion of the gel goes on for some time after the bead has escaped and moved away. Remarkably, these events do not occur in the case of vesicles: the outer rear and sides of the actin shell remain unaltered during the expulsion of the GUV, and afterwards (figure 3(C)). No macroscopic relaxation of the elastic stress in the actin gel is observed. These differences in the relaxation of the actin shells for beads and GUVs result in the different morphologies of their actin comet tails, as illustrated by movies 1 and 2 (available from stacks.iop.org/NJP/10/025001/mmedia) as well as the images in figures 1 and 2.

### 3.3. Surface fluidity imposes a minimal step-size in saltatory motion

The average step-size $d_V$ of saltatory vesicles was analyzed as a function of their diameter. Several thousands of saltatory vesicles of different diameters were tracked in the motility
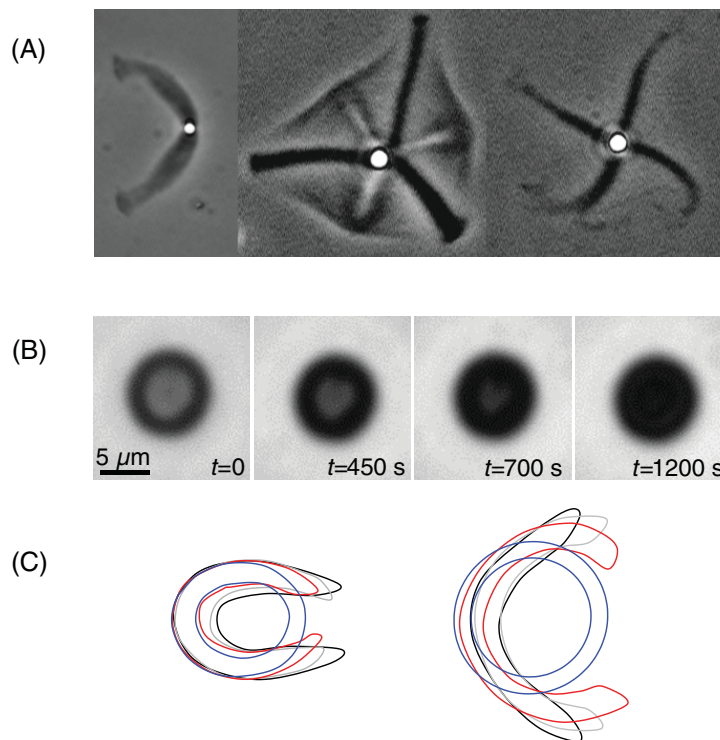
**Figure 3.** Symmetry-breaking for beads and vesicles, and evolution of the actin shell. (A) Beads ($2\,\mu$m in diameter) functionalized with a high surface density of N-WASP (corresponding to an average distance of $\sim$ 2–3 nm between N-WASP molecules) generate actin shells that break into multiple comet tails [26]. (B) A GUV collapses under the pressure of the growing actin shell when the surface density of N-WASP is high. (C) The actin shell expands after expulsion of a bead, in contrast with the vesicle case. The shape of the actin shell is plotted for the GUV (left) and the bead (right) studied in figure 1, at different times of the saltatory cycle: blue lines represent the closed shapes (defined as time zero), and red, gray and black curves correspond to times 80, 160 and 320 s for the vesicle, and 50, 100 and 250 s for the bead. Note that, during GUV expulsion, the outer rear boundaries of the actin shell superimpose, while the inner rear boundaries move forward, consistent with a twofold increase in the thickness of the actin gel as it grows inward. In contrast, during bead expulsion, the actin shell opens without thickening. It keeps on opening after the bead has moved away.

assay. The step-size increased quasi-linearly with the diameter of the vesicles (figure 4(A)), in agreement with Trichet *et al* [13], irrespective of the biochemical composition of the medium (different symbols in figure 4(A) correspond to different concentrations of proteins). Kinetic data (figure 1(A)) confirm that a GUV undergoing saltatory movement escapes rapidly out of the actin shell that surrounds it, and comes to a halt once it is outside. This observation suggests that the step-size is at least equal to the vesicle diameter, as verified in figure 4(A) (dashed line). A more accurate estimation of the minimal step-size is based on the following.
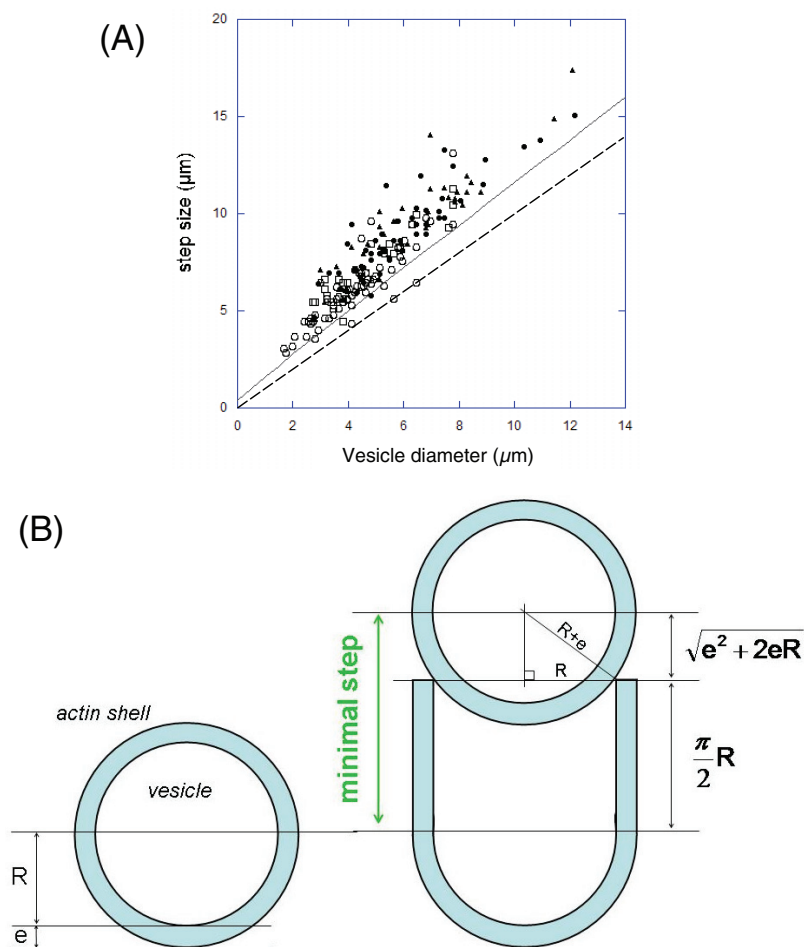
**Figure 4.** The step-size of saltatory GUVs increases quasi-linearly with GUV diameter, while remaining larger than the computed minimal step-size. (A) Step-size for vesicles undergoing saltatory movement, versus vesicle diameter, in various biochemical conditions: 25 nM Arp2/3 and 50 nM gelsolin (triangles), 25 nM Arp2/3 and 100 nM gelsolin (squares), 100 nM Arp2/3 and 50 nM gelsolin (filled circles), and 250 nM Arp2/3 and 100 nM gelsolin (open circles). Each data point corresponds to one vesicle; for clarity, only a representative subset of the thousands of observed vesicles is shown here, and error bars (typically 0.3 $\mu$m for both diameter and step-size) have been left out. The dashed line corresponds to a step-size equal to the vesicle diameter. The solid line corresponds to the computed minimal step-size depicted in (B). (B) Schematic representation of the minimal step-size of a vesicle during saltatory motion. The step-size is the distance between the rear position of two subsequent actin shells. It corresponds to the distance travelled by the vesicle center of mass between the times at which two consecutive actin shells (left and right panels) have reached the critical thickness. Note that the situation drawn on the right is identical to the real case ($t = 530$ s in figure 1(A)).

The smallest possible step corresponds to the case where the vesicle stops directly after escaping its actin shell, hereby positioning the new actin shell in contact with the previous one. The minimum step-size therefore depends only on the shape of the open actin shell. As illustrated in figure 3(C), the outer aspect of the actin shell's rear remains unchanged during this process, while at the front, the hole widens and its neck elongates as the GUV is progressively pushed through it. We can compute a lower limit of the step-size by leaving out neck elongation (due to actin polymerization) and considering only the deformation of the actin shell (which has an inner radius $R$ and an outer radius $R+e$, $e$ being the shell thickness) as it opens up. As shown in figure 3(C), the actin shell does not open up beyond what is necessary to make way for the GUV, hence the maximal hole radius is that of the GUV. As we show in the supplementary material (available from stacks.iop.org/NJP/10/025001/mmedia), smaller openings of the actin shell result in larger step-sizes. Hence the situation sketched in figure 4(B) corresponds to the minimal step-size, which can be computed based on simple geometrical considerations. The resulting minimal step-size varies quasi-linearly with the vesicle diameter $D$ like $\sqrt{eD+e^2}+(\pi/4)D$. Based on phase contrast microscopy images, we have measured the thickness $e$ of the actin shell at the onset of symmetry breaking. Remarkably, $e$ is identical at each step and increases linearly with the vesicle diameter (over the 2–12 $\mu$m range considered in this study) as described by the following equation: $e = 0.087D + 0.38\,\mu$m (determined by a linear fit of experimental data). The resulting minimal step-size is shown in figure 4(A) (solid line).

The fact that the step-size, measured over thousands of GUVs in saltatory movement, was always larger than the computed minimal step size (figure 4(A)) supports the view that the minimal step-size is determined by the opening of the actin shell: in the case of beads, the actin shell opens up to greater extents (figure 3(C)), and the new actin shell can be formed closer to the previous one, resulting in smaller step-sizes (figure 5).

### 3.4. Confinement hinders bead propulsion

Step-size measurements were also carried out on N-WASP coated beads in saltatory motion, to challenge the proposal that the large-scale relaxation of the gel away from the bead is required for movement. All data shown here (figure 5) were obtained under the same biochemical conditions as above for GUVs (50 nM Arp2/3 and 100 nM gelsosin). We found that the thickness of the sample (distance between slide and coverslip) affected the saltatory motion of microbeads: thin samples favor the occurrence of saltatory motion, and reduce the step-size (figure 5(A) and (B)). Figure 5(A) shows the step-size $d_B$, averaged over a set of beads, as a function of the sample thickness $h$. Independent of the bead diameter $D$, $d_B$ increased with sample thickness when the thickness was up to 2–2.5$D$, and reached a higher limit when samples were thicker. When thickness is less than 1.5$D$, the bead moved in short hops, with a step-size lower than the bead diameter.

In order to see if the proximity of one sample boundary was enough to affect step-size, we monitored saltatory propulsion of beads (diameter of $6.10 \pm 0.57\,\mu$m) located at different distances from the coverslip and the slide in a 25-$\mu$m-thick sample. Since beads do not remain at a constant distance from these surfaces as they move, only the most recent step was used to compute the step-size of each bead. Figure 5(C) shows that the step-size is independent of the position of the bead in the sample, even when in close proximity to either surface (less than one diameter away). Therefore, the observed dependence of saltatory behavior on sample thickness is due to the confinement of the bead between close slide and coverslip.
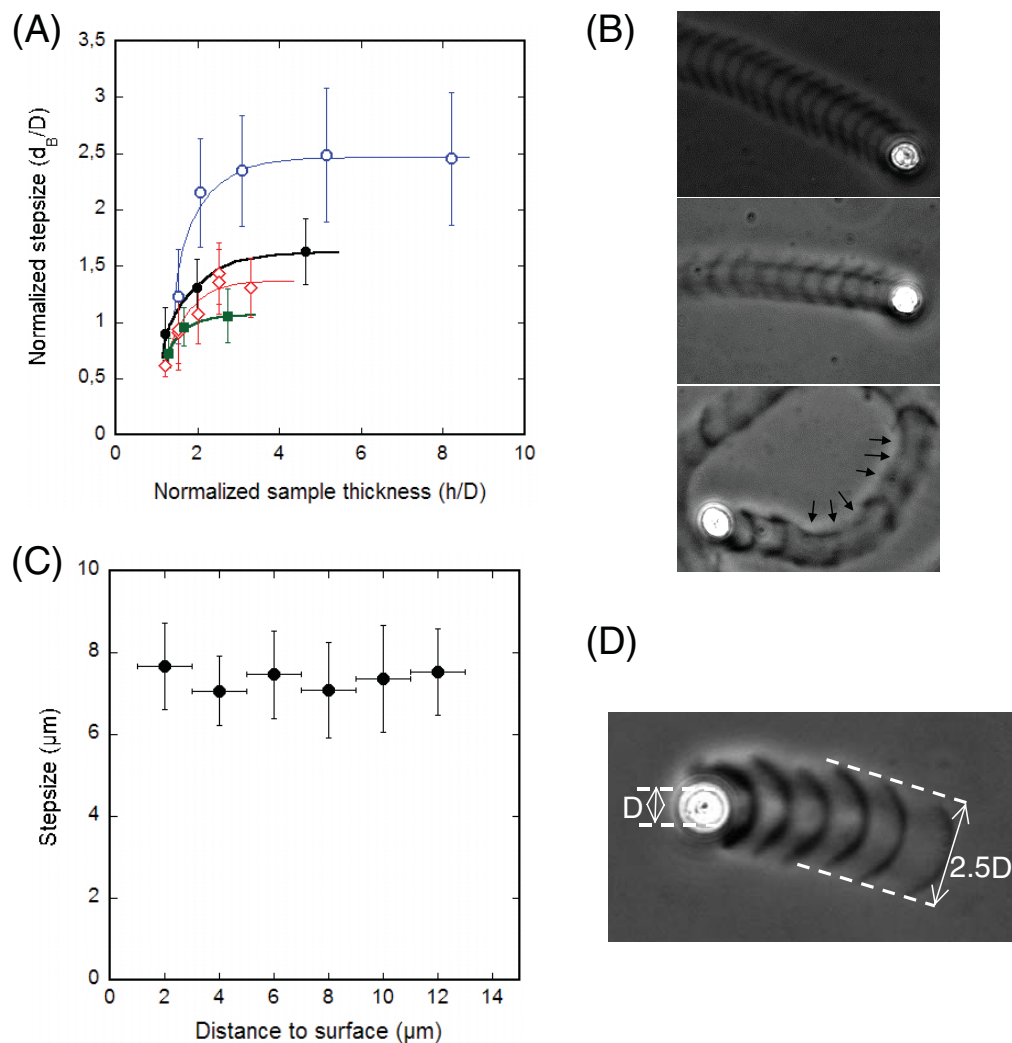
**Figure 5.** The step-size of saltatory beads depends on sample thickness. (A) The average step-size of beads of different diameter ($3.01 \pm 0.11$, $4.65 \pm 0.26$, $6.10 \pm 0.57$ and $9.29 \pm 0.85\,\mu m$ from top to bottom curve, respectively) was measured as a function of sample thickness. Step-size and thickness were normalized by the bead diameter. The step-size is independent of the sample thickness above a threshold thickness that is 2–2.5 times larger than the bead diameter. Error bars indicate standard deviations. (B) Top to bottom: 9.3-$\mu$m-diameter beads displayed increasing step-sizes of $6.3 \pm 0.8$, $8.7 \pm 0.8$, and $11.4 \pm 1.7\,\mu m$ (mean $\pm$ SD) in samples of increasing thickness ($\sim$12, 15 and 25 $\mu$m, respectively). In the thickest sample, the poor visibility of the steps (indicated by arrows) is due to positioning of the comet out of the focal plane. (C) The step-size of 6.1-$\mu$m-diameter beads in a 25-$\mu$m-thick sample is not affected by the distance between the bead and the nearest surface. The average bead step-size was equal to $7.36 \pm 0.24\,\mu m$, independent of the $z$-position of the bead. (D) Phase contrast image of a 10.5 $\mu$m-diameter bead undergoing saltatory movement in a $\sim$ 40-$\mu$m-thick sample. The opened actin shells are twice as large as the bead diameter. Note that in (B) and (D) the beads can appear larger than their actual diameter due to saturation in phase contrast imaging.

In contrast with the steady shape of the actin shell following the expulsion of a vesicle, the shell from which a solid bead escapes opens wide and goes on expanding after the bead has moved out (figure 3(C)). The critical threshold thickness of 2–2.5$D$, below which step-size decreases, corresponds exactly to the width of the fully opened actin shell (figure 5(D)). Therefore, by mechanically limiting the opening of the actin shell in one direction (the $z$-direction, perpendicular to the plane of movement) the propulsion of the bead is hindered, even if the opening of the actin shell is sufficient for the bead to move forward. The higher the constraints imposed against full opening of the actin shell, the lower the distance traveled by the bead before it stops (lower step-size). Wider comets were observed in thin samples (comets observed for 6.1 $\mu$m beads appeared 1.4 times wider in a 7.5 $\mu$m thick sample than in a 15 $\mu$m thick sample), consistent with the view that gel relaxation is limited in the $z$-direction.

In a previous study, Bernheim-Groswasser *et al* [9] observed a similar hopping propulsion of microbeads. Some features however differed from our observations. In that study, hopping beads had a sharper and lower ($\sim 1\,\mu$m min$^{-1}$) velocity peak. More importantly, large, densely-coated beads displayed a hopping movement, with a small step-size, in samples 5–6 times thicker than the bead diameter, while this behavior was observed here only in thin samples. Microbead protein densities and diameters, as well as motility medium composition, were similar in the two studies (in fact, we have repeated our experiments using the same protein concentrations as in [9] and observed the same behavior as reported in the present paper). The only significant experimental differences are that Bernheim-Groswasser *et al* used polystyrene beads coated with GST-tagged VCA (active sub-domain of N-WASP), while we use carboxylated polysterene beads coated with His-tagged N-WASP. Bernheim-Groswasser *et al* [9] showed that the hopping behavior of beads can be described assuming a non-monotonous friction force–velocity relation at the bead–actin gel interface. The fact that we observe a dominant hopping behavior with a small step-size in thin samples suggests either that the compression of the actin gel by the sample walls has an impact on the force–velocity relation at the bead–gel interface, or that a new independent mechanism is responsible for hopping.

## 4. Mobility of nucleators on the surface alters comet tail structure and the relaxation of elastic stress in the actin gel

The putative role of stress relaxation within the actin gel during continuous movement was examined as follows. A two-fluorophore experiment was carried out, as described by Paluch *et al* [20] (see appendix) to monitor the relaxation of the actin gel after detachment from the particle surface (figure 6). For beads, the boundary separating the two fluorescently labeled actins in the tail was wider than the bead diameter and was less curved, meaning that the actin gel deformed and expanded continuously following its synthesis at the bead surface, in agreement with previous reports [20]. No such deformation of the actin layers can be detected in the comet tail generated by GUVs. This behavior persisted over the large range of vesicle diameter (from 4.7 to 15 $\mu$m) and deformation (deformation ratio $L/D$ from 1.10 to 1.32) that we observed. Hence, the differences in stress relaxation of the actin meshwork that are displayed by beads and GUVs in symmetry breaking and saltatory movement persist during continuous movement.

These results can be understood as follows. The homogeneous distribution of immobilized N-WASP on the bead surface induces the formation of an actin gel at the front. The macroscopic
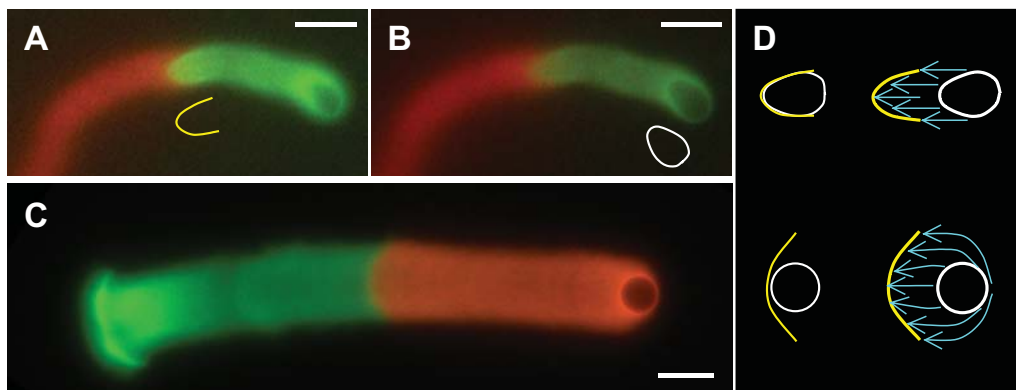
**Figure 6.** The actin gel exhibits large-scale relaxation following its detachment from a rigid spherical surface, but not following its detachment from a fluid vesicle. The relaxation of the actin tail behind a vesicle (A and B, focused on the color transition in the actin tail, and the vesicle, respectively) and a bead (C) was observed using actin labeled with Alexa-568 (in red) and Alexa-488 (in green), based on a protocol from Paluch *et al* [20]. The profiles of the boundary between the red and green regions in the actin tails are redrawn on panel D (yellow line). It superimposes the GUV contour (white line), but does not superimpose the bead contour, indicating that large-scale stress relaxation in the actin gel takes place during bead propulsion, but not during GUV propulsion. The blue arrows indicate the motion of the actin meshwork after polymerization at the surface. Scale bar $= 10 \, \mu$m.

relaxation of stress in the actin gel accompanies the movement of this portion of the gel from the front of the bead to the sides of the comet tail, as the bead moves forward (figure 6(D)). In contrast, N-WASP is inhomogeneously distributed at the surface of actin-propelled GUVs [14]–[16] with a lower density at the front (similarly to previous observations on other fluid objects [12, 13]). The density of N-WASP at the front of the GUV therefore falls below the threshold required for building a cohesive network, and no large-scale relaxation of the actin gel is observed in that case (figure 6(D)). Elastic stress may nonetheless relax in the actin gel around GUVs, especially when they are deformed [12]. However, actin-based propulsion of GUVs is not strictly dependent on their deformation, since some GUVs remain quasi-spherical as they move (figure 7(B)). In contrast, N-WASP segregation is always linked to actin-based propulsion of GUVs.

The asymmetry in N-WASP distribution, during GUV continuous propulsion, was quantified using fluorescently labeled proteins, and by computing a segregation ratio $r_s$ (see appendix: $r_s > 0.5$ indicates segregation at the rear). We measured a N-WASP segregation ratio of $0.59 \pm 0.04$ on continuously moving vesicles (ranging from 4.35 to 12.05 $\mu$m in diameter, in a standard motility medium containing 100 nM gelsolin and 100 nM Arp2/3 complex). On microbeads, no segregation of N-WASP was detected ($r_s = 0.50 \pm 0.01$), confirming that N-WASPs is strongly adsorbed and does not dissociate from the bead surface during symmetry-breaking. The distance between N-WASP molecules decreased typically to $\sim 19$ nm (see appendix) at the vesicle rear point, lower than the average distance of 23 nm measured for homogeneous distribution. However it never decreased below 15 nm, indicating that the local N-WASP density is always lower on GUVs than on beads, even when N-WASP is segregated.
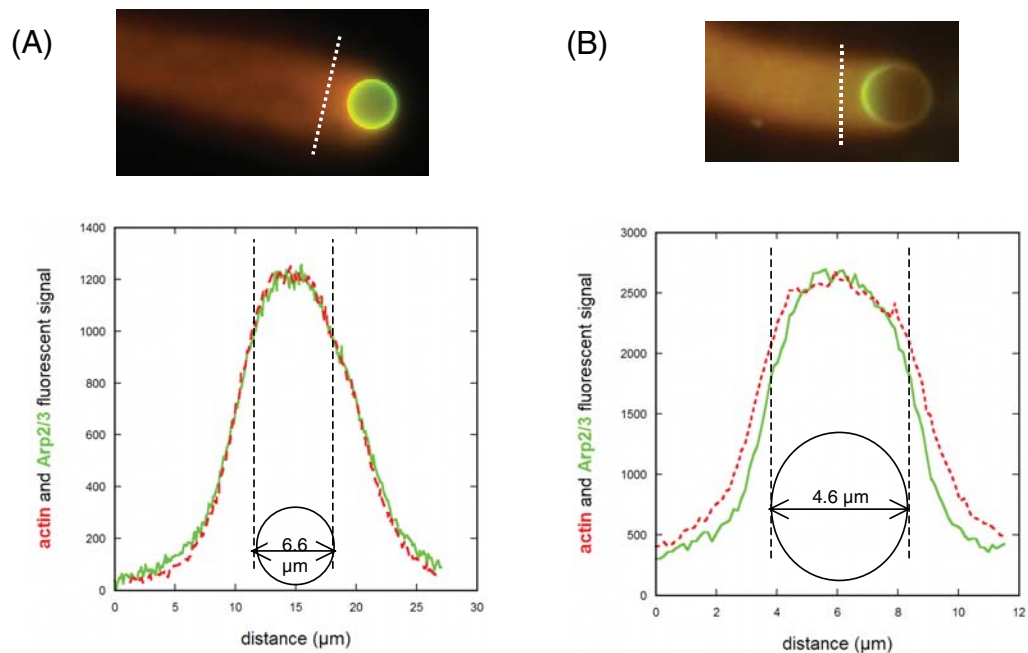
**Figure 7.** Comet tail structure. Fluorescence microscopy images, showing actin (in red) and Arp2/3 complex (in green) for a $6.6 \, \mu m$ bead (A) and a $4.6 \times 5.0 \, \mu m$ vesicle (B) undergoing continuous propulsion. Arp2/3 segregation is readily visible on the vesicle, not on the bead. The fluorescence profiles of actin (red) and Arp2/3 (green) were measured across the actin tails, along the white dashed lines. For the bead, the intensity profiles of actin and Arp2/3 are superimposable, meaning that the branching density is constant across the tail section. For the vesicle, the actin profile is wider than the Arp2/3 profile, indicating a 50% higher branching density in the center of actin tail than at the sides. The bead and vesicle shapes drawn on the intensity profiles show the difference between the cross-section of the actin tail and of the particles.

To investigate the impact of N-WASP segregation at the vesicle rear on the structure of the actin tail, we also monitored the distribution of Arp2/3 and actin on the particle surface and in the actin tail. Both proteins co-segregated with N-WASP and displayed a higher density at the rear of the GUV, at the interface with the actin tail, with segregation ratios higher than that of N-WASP ($0.69 \pm 0.04$ and $0.72 \pm 0.07$ for Arp2/3 and actin, respectively). The co-localization of N-WASP, Arp2/3 and actin at the rear of the moving GUVs reflects the two functional states of N-WASP which either diffuses freely or interacts with actin filaments via Arp2/3 upon branching [13, 14]. Under the same biochemical conditions, on the surface of continuously propelled beads, Arp2/3 was homogeneously distributed like N-WASP. Actin, however, segregated much less at the rear of beads than on GUVs ($r_s = 0.59 \pm 0.02$), confirming that filaments are generated by N-WASP at the bead front.

In the regime of continuous propulsion, the comet tails of beads and GUVs also show different morphologies and structural organization at the molecular level (figure 7). The actin density in the tail is 2–4 times higher for beads than for GUVs, certainly due to the higher average surface density of N-WASP on beads. Moreover, we observed that the tail diameter exceeds the size of the particle diameter to a greater extent for beads than for vesicles

**IOP** Institute of Physics $\Phi$ DEUTSCHE PHYSIKALISCHE GESELLSCHAFT

(figures 6 and 7), consistent with the observation that a significant number of filaments is generated at the bead front, and that the incorporation of these filaments into a meshwork around the bead (figure 6(D)) eventually thickens the actin tail. The segregation of N-WASP at the GUV surface greatly weakens and may abolish this effect.

Both beads [11] and GUVs [14] show a constant branching density along the axis of the tail. In contrast, when recorded along a cross-section of the actin tail, the branching density is constant for beads, while for GUVs it is typically 50% higher in the inner than in the outer region of the actin tail (figure 7). This local increase in branching frequency is consistent with the segregation of N-WASP at the rear of the GUV. These observations provide the first experimental support to the idea that the ratio of pulling to pushing filaments is greater at the rear of the GUV.

## 5. Discussion and conclusion

In the present work, we have analyzed the main features of saltatory and continuous actin-based propulsion of functionalized solid beads or lipid vesicles. We compared the phenotypes of symmetry-breaking, the structural organization of the actin tails at the molecular level and the distribution of nucleators at the surface. We come to the conclusion that hard and fluid actin-propelled objects rely on different mechanisms to establish and maintain directed movement. Large-scale stress relaxation (deformation) of the actin gel grown from a bead is necessary for movement, and provides a way to evacuate the actin filaments that are grown in front of the bead. The accumulation of actin at the front of the bead would jeopardize its movement, and large-scale stress relaxation can be seen as a way to maintain anisotropy in the system. In the case of a motile GUV, anisotropy is present at the surface since N-WASP is segregated at the rear. This anisotropy is necessary for directed movement. No significant amount of actin polymerization takes place at the front of the GUV, and no large-scale stress relaxation is observed. Hence, N-WASP segregation and large-scale stress relaxation can be viewed as the two different mechanisms used respectively by fluid and hard objects to establish and maintain the anisotropy necessary for directed movement. According to these results, we expect that the large-scale relaxation of the actin gel would not be required for propulsion of solid beads asymmetrically coated with N-WASP.

The hopping movement of VCA-coated oil droplets, recently reported by Trichet *et al* [13], bears similarities with the hopping movement of GUVs presented here. However, in the case of oil droplets, the peak in velocity occurs later in the cycle, once the droplet has nearly relaxed back to a quasi-spherical shape, and the step-size is smaller. These differences certainly stem from the different mechanical properties of the two types of surfaces (lipid bilayer and oil–water interface), as well as differences in the interaction of these surfaces with the actin gel. Possible relevant causes include the biochemical/catalytic properties of the nucleators (N-WASP and VCA), the nature of their attachment to the surface (His-tag on Ni-lipids and adsorption on the oil surface), and the kinetics of their detachment from actin filaments (involving the regulatory effect of VASP in the case of oil droplets). The confinement-sensitive hopping movement of microbeads that we present here exhibits significant differences with the hopping movement of microbeads reported by Bernheim-Groswasser *et al* [9], probably also in connection with differences in the interaction between the bead surface and the actin gel, and possibly leading to a different mechanism.

The simple biomimetic model systems used here (solid beads and soft liposomes) can be viewed as the two extremes of the range of surfaces on which site-directed actin assembly

produces force in living cells. Real biological membranes can be more rigid than synthetic liposomes, and can present additional heterogeneity in their mehanical properties caused by the insertion of protein assemblies in which regulated N-WASP might be integrated. It is anticipated that the regulation of the mechanical properties of biological membranes will affect the dynamics of the actin cytoskeleton and determine the motile behavior and morphology of shape changes [28].

## Acknowledgments

## Appendix A. Materials and methods

### A1. Proteins

Actin was purified from rabbit muscle according to the protocol of Spudich and Watt [29] and labeled with either rhodamine-NHS or Alexa-488 or Alexa-568 succinimidyl ester [30]. Recombinant human ADF and gelsolin were expressed in *Escherichia coli* [5]. Profilin was purified from bovine spleen [31]. Arp2/3 complex was purified from bovine brain [32] and labeled with Alexa-488 maleimide. Human His-tagged N-WASP was expressed in Sf9 cells using the baculovirus system [32] and labeled with Alexa-488 maleimide [11].

### A2. Functionalization of microbeads

Carboxylated polystyrene beads of varying diameter (monodisperse solutions, diameter from 2 to $9.3 \, \mu$m, Polysciences) were incubated for 1 h on ice in X buffer (10 mM Hepes pH 7.8, 0.1 M KCl, 1 mM $MgCl_2$, 1 mM ATP, 0.1 mM $CaCl_2$ and 0.01% $NaN_3$) containing 400 nM of N-WASP. The volume of beads was adjusted so that the total solid surface area remained constant, independently of the bead diameter. BSA (1% (w/v)) was added for 15 min. Beads were washed in X buffer and finally stored in X buffer supplemented with 0.1% BSA. The functionalized beads were stored on ice and used for up to 2 weeks without any noticeable change in their properties.

### A3. Preparation of GUVs

1,2-Dioleoyl-sn-glycero-3-phosphocholine (DOPC) and 1,2-dioleoyl-sn-glycero-3-[(N-(5-amino-1-carboxypentyl)iminodiacetic acid)succinyl] nickel salt (DOGS-NTA-Ni) were purchased from Avanti Polar Lipids and stored at $-20\,°$C as chloroformous solutions (10 mg ml$^{-1}$ for DOPC, 5 mg ml$^{-1}$ for DOGS-NTA-Ni). Mixtures of DOPC and DOGS-NTA-Ni in a 9 : 1 mol : mol ratio were prepared and stored for one month at $-20\,°$C.

GUVs were prepared by electroswelling. The electroformation technique was optimized to obtain 5–10 $\mu$m GUVs in roughly 20 min instead of 3–4 h [14]. The vesicles were stored on ice for 2–3 weeks.

### A4. Motility assays

*A4.1. Vesicle motility assay.* The vesicle suspension was diluted 5- to 10-fold in swelling buffer containing 400 nM N-WASP. After 2 h incubation, vesicles were diluted 10-fold in the motility medium. The vesicle motility medium was optimized from standard motility medium designed for solid beads [11] and consisted of 13.5 $\mu$M F-actin, 2.4 $\mu$M profilin, 100 nM gelsolin, 50 nM Arp2/3, 4 $\mu$M ADF in glucose buffer (5 mM Tris pH 7.8, 60 mM KCl, 2 mM MgCl$_2$, 2 mM ATP, 0.1 mM CaCl$_2$, 1% (w/v) BSA, 0.1% (w/v) methylcellulose, 0.01% NaN$_3$, 1 mM DTT, 0.5 mM DABCO, 65 mM sucrose and 90 mM glucose). Changes are indicated in the text. The proteins were mixed at least for 10 min at room temperature, to reach the steady state of actin assembly, before addition of the vesicles. Vesicles were observed between microscopy slide and coverslip, in thick chambers drawn using a hydrophobic pen (Dakocytomation) and sealed with Valap (vaselin : lanolin : paraffin 1 : 1 : 1). The chamber depth ($\sim 80$–$100\,\mu$m) was set by the hydrophobic walls. The samples were observed either in phase contrast or fluorescence microscopy.

*A4.2. Bead motility assay.* The motility medium for beads consisted of a solution of 7 $\mu$M F-actin, 4.5 $\mu$M ADF, 2.4 $\mu$M profilin, 100 nM gelsolin and 50 nM Arp2/3 complex in X buffer, supplemented with 1% BSA, 4 mM MgCl$_2$, 2 mM ATP, 150 $\mu$M DABCO and 6.7 mM DTT. Changes in the medium are indicated in the text. A few microliter were placed between microscope slide and coverslip ($18 \times 18$ mm$^2$) and sealed with Valap (vaselin : lanolin : paraffin 1 : 1 : 1). The sample thickness could be varied by changing the volume of the sample. The calculated value of the thickness was found to agree with the sample thickness measured under the microscope, by focusing on the two surfaces. The samples were observed either in phase contrast or fluorescence microscopy.

Phase contrast imaging was performed using a Nikon Diaphot microscope equipped with a 20x air objective (NA 0.5), a motorized stage (Märzhäuser) and a CCD camera (Orca II ERG, Hamamatsu). Fluorescence imaging was performed using an Olympus AX70 microscope equipped with a 60x immersion objective (NA 1.42), a motorized stage (Märzhäuser) and either an EMCCD camera (Cascade II:512, Photometrics) or the Orca II ERG CCD camera. MetaMorph 6.3 software (Universal Imaging Corp.) was used for image acquisition, stage control and the Olympus microscope control. Image analysis was carried out using Image J or Metamorph software.

### A5. Measurement of the step-size of saltatory beads and vesicles

For both vesicles and beads, the average step-size was measured as a function of the object diameter, using phase contrast microscopy. For vesicles, the maximum number of steps in the comet (integer $N$) and the distance $L$ (along the comet) between the first and the last dense actin regions were measured. The average step-size was calculated as $L/N$. The vesicle diameter $D$ was defined as the diameter of the spherical vesicles, and as the average between the long and short axis of deformed vesicles. For beads, the step-size of saltatory beads of different diameter was measured with different sample thicknesses. For a fixed sample thickness and fixed bead size, the saltatory comets of a few tens of beads were imaged in phase contrast microscopy. Each size of each step was measured and the average step-size was computed from all the measurements done in one sample. When measuring the step-size of beads as a function of the

distance to the nearest surface (in a thick sample), the position of the bead was given by the stage position when the bead was in focus. The size of the latest step was measured.

### A6. Measurement of N-WASP density on the surface

The average N-WASP surface density on beads was determined by SDS PAGE and immunoblotting as described in [11]. The fluorescence intensity of N-WASP on GUVs was compared to that measured on beads, and the local surface density was derived.

### A7. Measurement of the protein distribution at the surface

Labeled actin, N-WASP and Arp2/3 were used to monitor their distribution at the surface of the actin-propelled objects. In the case of Arp2/3, the contribution of Arp2/3 present in the actin gel at the vicinity of the GUV surface was estimated and substracted. We computed a 'segregation ratio' $r_s$ defined as the sum of the fluorescence intensity of the protein over the rear half of the object contour (towards the actin tail), divided by its sum over the whole contour. A segregation ratio of 0.5 corresponds to a homogeneous distribution; a segregation ratio above 0.5 means that the protein density is higher at the rear of the object.

### A8. Measurement of the branching density in the actin tail

The relative densities of actin and Arp2/3 complex in the actin comets were evaluated using rhodamine- or Alexa-568-labeled actin and Alexa-488-labeled Arp2/3 complex in the motility medium. The rhodamine/Alexa-568 and Alexa-488 fluorescence intensities were measured across the actin tails using Metamorph software. The ratio of the intensities of Arp2/3 to actin represents the density of branching in the actin comet.

### A9. Observation of GUV symmetry-breaking

Functionalized GUVs were incubated in a motility medium containing 0.3% Alexa-488-labeled actin for 15 min. GUVs were then placed in a motility medium of identical composition, except for 0.2% Alexa-568-labeled actin, and observed for 30 min. The actin gel polymerized before mixing contained Alexa-488-actin only, while the actin gel polymerized after mixing contained both fluorophores. The profiles of Alexa-568 (red) and Alexa-488 (green) fluorescence were plotted along the direction of symmetry-breaking ($x$-axis in figures 2(B) and (C)). The red fluorescence came from the actin gel that polymerized after mixing (i.e. the inner region). The green signal came from the whole actin gel (i.e. regions polymerized before and after mixing). The contribution from the actin gel polymerized after mixing was determined using the red signal, and a reference was provided by actin-propelled vesicles displaying comet tails polymerized after mixing. This allowed the amount of green fluorescence coming from the actin gel polymerized before mixing (i.e. the outer region) to be computed.

For each region of the gel, two peaks were measured, corresponding to the rear and the front of the actin shell. The thickness of each region was determined by directly measuring the peaks' width at half maximum (taking the signal between the peaks as a base), and alternatively by fitting the peaks by gaussians (taking zero as a base). Both methods gave the same quantitative results regarding the front-to-rear thickness ratio.

*A10. Measurement of the relaxation of the actin tail*

The evolution of the actin tail during its growth from the surface of the bead or GUV was monitored using successively two differently labeled actin, according to the technique described by Paluch *et al* [20]. The extent of relaxation of the actin gel following its detachment from the functionalized surface was evaluated by comparing the curvatures of the particle and of the boundary between the two differently labeled regions of the actin tail.

## References

[1] Kaksonen M, Toret C P and Drubin D G 2006 *Nat. Rev. Mol. Cell Biol.* **7** 404
[2] Rottner K, Stradal T E and Wehland J 2005 *Dev. Cell* **9** 3
[3] Small J V, Stradal T, Vignal E and Rottner K 2002 *Trends Cell Biol.* **12** 112
[4] Takenawa T and Suetsugu S 2007 *Nat. Rev. Mol. Cell Biol.* **8** 37
[5] Loisel T P, Boujemaa R, Pantaloni D and Carlier M-F 1999 *Nature* **401** 613
[6] Pantaloni D, Le Clainche C and Carlier M-F 2001 *Science* **292** 1502
[7] Borisy G G and Svitkina T M 2000 *Curr. Opin. Cell Biol.* **12** 104
[8] Mogilner A 2006 *Curr. Opin. Cell Biol.* **18** 32
[9] Bernheim-Groswasser A, Prost J and Sykes C 2005 *Biophys. J.* **89** 1411
[10] van der Gucht J, Paluch E, Plastino J and Sykes C 2005 *Proc. Natl Acad. Sci. USA* **102** 7847
[11] Wiesner S, Helfer E, Didry D, Ducouret G, Lafuma F, Carlier M-F and Pantaloni D 2003 *J. Cell Biol.* **160** 387
[12] Boukellal H, Campas O, Joanny J F, Prost J and Sykes C 2004 *Phys. Rev.* E **69** 061906
[13] Trichet L, Campas O, Sykes C and Plastino J 2007 *Biophys. J.* **92** 1081
[14] Delatour V, Helfer E, Didry D, Lê K H D, Gaucher J-F, Carlier M-F and Romet-Lemonne G *Biophys. J.* submitted
[15] Giardini P A, Fletcher D A and Theriot J A 2003 *Proc. Natl Acad. Sci.* **100** 6493
[16] Upadhyaya A, Chabot J R, Andreeva A, Samadani A and van Oudenaarden A 2003 *Proc. Natl Acad. Sci.* **100** 4521
[17] Taunton J, Rowning B A, Coughlin M L, Wu M, Moon R T, Mitchison T J and Larabell C A 2000 *J. Cell Biol.* **148** 519
[18] Carlier M F and Pantaloni D 1997 *J. Mol. Biol.* **269** 459
[19] Mogilner A and Oster G 2003 *Biophys. J.* **84** 1591
[20] Paluch E, van der Gucht J, Joanny J-F and Sykes C 2006 *Biophys. J.* **91** 3113
[21] Gerbal F, Chaikin P, Rabin Y and Prost J 2000 *Biophys. J.* **79** 2259
[22] Cameron L A, Robbins J R, Footer M J and Theriot J A 2004 *Mol. Biol. Cell* **15** 2312
[23] Paluch E, van der Gucht J and Sykes C 2006 *J. Cell Biol.* **175** 687
[24] van Oudenaarden A and Theriot J A 1999 *Nat. Cell Biol.* **1** 493
[25] Sekimoto K, Prost J, Julicher F, Boukellal H and Bernheim-Grosswasser A 2004 *Eur. Phys. J.* E **13** 247
[26] Wiesner S 2003 *PhD Thesis* University of Paris XI
[27] Heuvingh J, Franco M, Chavrier P and Sykes C 2007 *Proc. Natl Acad. Sci. USA* **104** 16928
[28] Ridley A J 2006 *Trends Cell Biol.* **16** 522
[29] Spudich J A and Watt S 1971 *J. Biol. Chem.* **246** 4866
[30] Isambert H, Venier P, Maggs A C, Fattoum A, Kassab R, Pantaloni D and Carlier M F 1995 *J. Biol. Chem.* **270** 11437
[31] Gutsche-Perelroizen I, Lepault J, Ott A and Carlier M F 1999 *J. Biol. Chem.* **274** 6234
[32] Egile C, Loisel T P, Laurent V, Li R, Pantaloni D, Sansonetti P J and Carlier M F 1999 *J. Cell Biol.* **146** 1319